Quantum Science and Technology

Celebrating the 10th anniversary of Quantum Science and Technology

PURPOSE-LED PUBLISHING™

PAPER • OPEN ACCESS

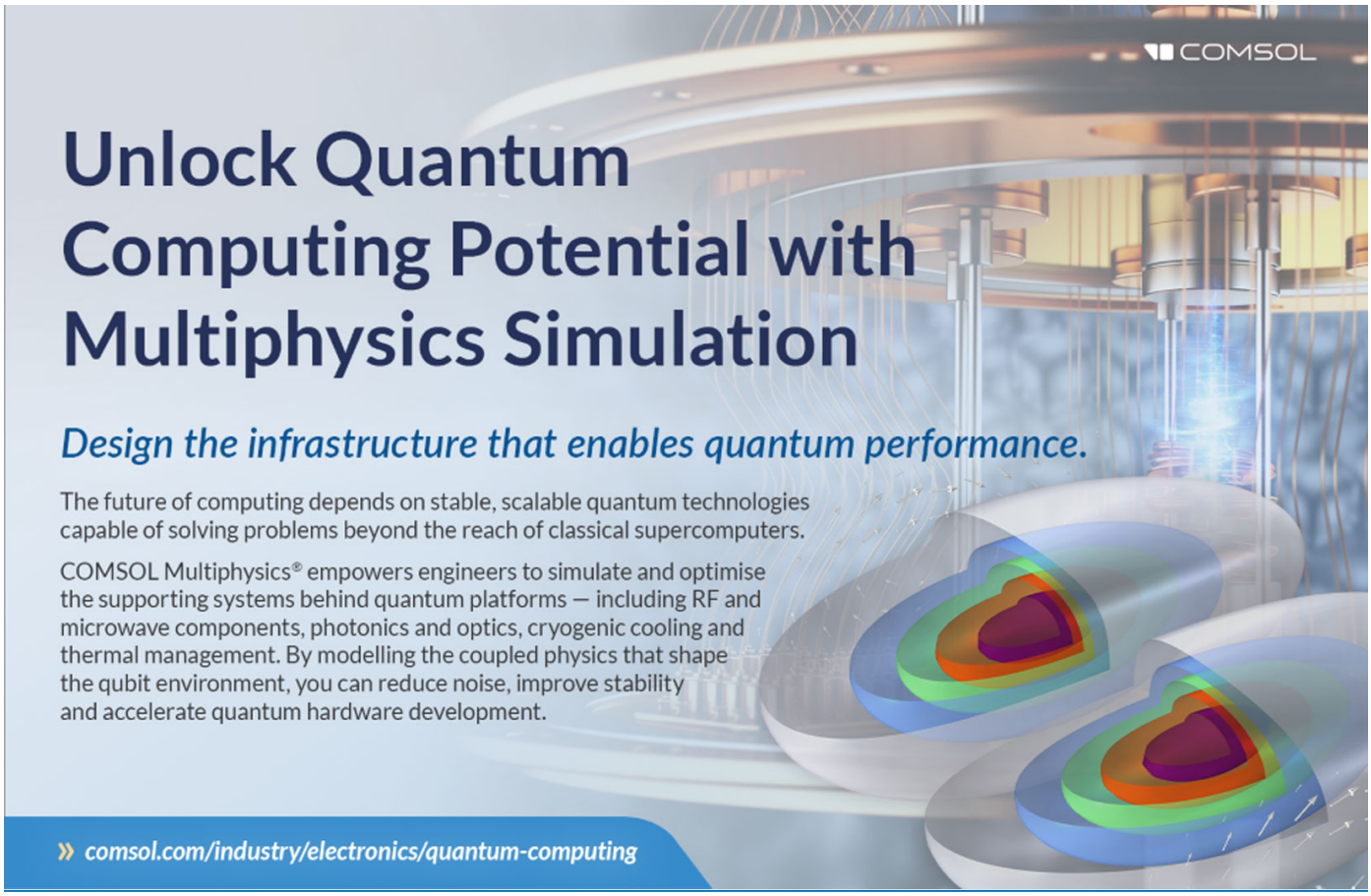
Complete coherent control of spin qubits in self-assembled InAs quantum dots under oblique magnetic fields

To cite this article: I Samaras *et al* 2026 *Quantum Sci. Technol.* **11** 045066

View the article online for updates and enhancements.

You may also like

- Spin manipulation in semiconductor quantum dots qubit
Ke Wang, , Hai-Ou Li et al.
- Observation of anticrossings in the exciton state of single quantum dots via electrical tuning of the fine-structure splitting
M A Pooley, A J Bennett, R M Stevenson et al.
- A review of the coherent optical control of the exciton and spin states of semiconductor quantum dots
A J Ramsay



This content was downloaded from IP address 130.159.24.160 on 07/10/2026 at 15:42

Quantum Science and Technology

Check for updates

OPEN ACCESS

RECEIVED
21 April 2026

REVISED
8 September 2026

ACCEPTED FOR PUBLICATION
17 September 2026

PUBLISHED
7 October 2026

Original content from this work may be used under the terms of the Creative Commons Attribution 4.0 licence.

Any further distribution of this work must maintain attribution to the author(s) and the title of the work, journal citation and DOI.



PAPER

Complete coherent control of spin qubits in self-assembled InAs quantum dots under oblique magnetic fields

I Samaras[1,*], K Barr[1], C Schneider[2], S Höfling[3] and K G Lagoudakis[1,*]

[1] University of Strathclyde, Glasgow G4 0NG, United Kingdom
[2] Institut für Physik, Fakultät V, Carl von Ossietzky Universität Oldenburg, 26129 Oldenburg, Germany
[3] Julius-Maximilians-Universität Würzburg, Technische Physik, 97074 Würzburg, Germany
[*] Authors to whom any correspondence should be addressed.

E-mail: ioannis.samaras@strath.ac.uk and k.lagoudakis@strath.ac.uk

Keywords: quantum dots, coherent control, spin physics, spin qubits, oblique magnetic fields

Supplementary material for this article is available online

Abstract

We demonstrate complete coherent control of a single spin qubit confined in a self-assembled InAs negatively charged quantum dot (QD) subjected to an oblique magnetic field, and directly compare this regime with the conventional Voigt geometry. In the oblique-field configuration, the ground-state spin eigenstates are found to be unequal superpositions of the bare electron spin, with their composition tunable via the orientation of the applied field. This tunable spin mixing provides an additional degree of freedom to engineer the spin basis and associated optical couplings in the charged QD system. Although this geometry has a distinct structure with important implications, it provides a regime in which we can fully and coherently control the tailored spin qubit. We observe Rabi oscillations and Ramsey fringes, and demonstrate arbitrary single-qubit rotations, enabling a direct comparison with the Voigt case. Our results establish that spin-qubit control does not necessarily require a pure Voigt geometry and can instead be achieved under oblique magnetic fields. This relaxes constraints on device and field alignment and offers a versatile route to design and optimise spin-photon interfaces and spin-based quantum information processing architectures in semiconductor QDs.

1. Introduction

Self-assembled quantum dots (QDs) are a leading solid-state platform for optical quantum technologies. Strong three-dimensional confinement produces discrete, atom-like energy levels with large oscillator strengths and near transform-limited optical transitions, enabling an extremely broad range of applications. When charged, these QDs host a single electron or hole spin that forms a long-lived ground-state qubit, optically accessed via trion transitions with well-defined selection rules for initialisation, control, and readout [1]. In addition, self-assembled QDs have supported a broad range of single-spin protocols, including spin pumping [2], coherent control [3–15], spin echo techniques [16], spin-photon interface [17, 18], spin-photon entanglement [19, 20] and are typically demonstrated in standard magnetic-field orientations like the Faraday [21] or Voigt configuration. In these standard geometries, coherent control is well established, and performance is typically constrained by acoustic phonon interactions [22], and charge noise [23] rather than the control mechanism itself. Magnetic fields tilted away from the Faraday or Voigt configurations provide additional degrees of freedom by exploiting traits from both geometries. This additional tunability is attractive because Faraday fields provide near-cycling transitions suited to high-fidelity optical readout, whereas Voigt fields yield the double-Λ structure commonly used for optical spin control. Related progress has recently been reported in Faraday geometry, where heavy hole-light hole mixing is used to realise a highly asymmetric Λ-system with cyclic optical transitions for spin control and readout [12]. In this work, we instead use an oblique magnetic field to engineer the spin basis and demonstrate universal all-optical control in a tilted-field regime. Thus, an oblique field, in principle,

© 2026 The Author(s). Published by IOP Publishing Ltd

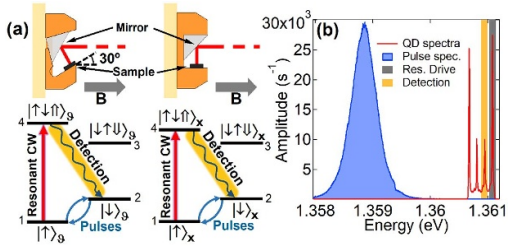


Figure 1. (a) Sample holders for oblique (left) and Voigt (right) along with the double-Λ systems for each one of the geometries. (b) Raw PL shows the excitation/detection scheme of our QD with the non-resonant pulses in the oblique geometry.

allows one to interpolate between these regimes and balance 'enough cycling' for readout with 'enough mixing' for control in a single static configuration [24]. Despite this promise, demonstrations of complete coherent control of single QD spin qubits, such as arbitrary SU(2) rotations validated by Rabi and Ramsey measurements, have largely been performed in the Voigt configuration, where the selection rules simplify giving rise to a double-Λ system with orthogonal linear polarisations for each branch [24, 25]. By contrast, tilted-field studies have focused predominantly on extracting g-tensor anisotropies [26–28], or on manipulating excitonic (bright/dark) manifolds [29–31], rather than investigating the resulting tailored ground-spin states [24] as an optically controllable qubit.

Here we close this gap by demonstrating complete coherent control of a charged self-assembled InAs QD in a fixed oblique magnetic field and compare it directly with the Voigt data acquired from the same QD. We show that a single pulsed laser can implement arbitrary qubit rotations even when the field is tilted away from both the Faraday and Voigt orientations. Despite the fact that the ultrafast rotations happen around an axis that is tilted away from the equatorial plane of the Bloch sphere, we observe clear Rabi oscillations and by carefully tuning the pulse power of a dual pulse train to the correct rotation angle, we observe Ramsey fringes. Finally, combining two rotations separated by a precisely timed delay, we realise general SU(2) rotations on the Bloch sphere. Our experimental findings are complemented by quantum optical simulations that capture the full complexity of the oblique field and show excellent agreement with the measured data. These results establish that universal all-optical single-qubit control is compatible with oblique magnetic fields in self-assembled QDs, linking the mature Voigt-geometry toolbox to the tilted-field configuration with its additional degrees of freedom.

2. Experimental details

2.1. Sample, cryogenic environment & magnet geometry

The experiments are performed in a self-assembled δ-doped InAs QD sample grown by molecular beam epitaxy in Stranski–Krastanow mode. The QD layer is positioned at the centre of a GaAs microcavity with 5 (24) top (bottom) Distributed Bragg Reflector $Al_{0.9}Ga_{0.1}As$/GaAs mirror pairs, which enhances both the directionality and the emission properties of the QDs. Charging of the QDs is promoted by a Si δ-doped layer (doping density $\sim 1.8 \cdot 10^{10}\,\mathrm{cm}^{-2}$) placed 10 nm below the QD layer, so that approximately one third of the dots are singly charged. The QDs investigated emit in the 910–920 nm range. More details of the sample structure can be found in [32]. The specific dot studied here is selected under above-band (Ab. Bd.) excitation at 780 nm by comparing spectra with and without the applied magnetic field and choosing a dot that exhibits the characteristic fourfold Zeeman splitting, an indication for charged QDs. The sample is mounted in a continuous-flow liquid-helium magneto-cryostat (Oxford Microstat-MO) with a helium cryorecirculator (ColdEdge Stinger), enabling stable closed-cycle operation while allowing the use of the integrated superconducting solenoid to generate a strong magnetic field [33]. The system provides a homogeneous magnetic field up to 5 T along the cryostat axis. Unless otherwise stated, measurements are performed at T = 5.0–5.5 K. For Zeeman-splitting measurements, the temperature is set to 6.5 K to reduce spectral drift during magnetic-field ramps caused by magnet/sample heating. To access the two magnetic field configurations studied here, two different custom-built sample holders are used. For the oblique geometry, the sample holder orients the sample at $\vartheta = 60°$ from Faraday geometry, while optical access is enabled using an appropriately tilted mirror in close proximity to the sample. The same principle is used for the Voigt geometry, where the angle is at $\vartheta = 90°$ as shown at the top of figure 1(a). The angle ϑ is defined with respect to the growth axis (Faraday).

2.2. All optical excitation & detection scheme

Optical excitation and collection are performed with a $0.5-$NA long-working-distance microscope objective (W.D. $= 12$ mm) producing a $\sim 1\,\mu$m (FWHM) spot on the sample. As the sample is static, we can access different areas of the sample surface by moving the microscope objective. We use a weak above band (Ab. Bd.) laser at 780 nm for initial characterisation, which is switched off during the main coherent control experiment. For all-optical coherent control we use pulses from an ultrafast Ti:sapphire laser with a repetition rate of at 80.2 MHz. The pulse duration in the sample is 3 ps (intensity FWHM), short compared to the trion lifetime ($\sim$0.8 ns). We spectrally shape and filter the off-resonant pulses so that their spectral centres are red-detuned by approximately $\sim$500 GHz from the targeted Λ-system under investigation, thereby minimising population transfer to the trion state [34]. In the oblique (Voigt) configuration we initialise the qubit by resonantly driving the highest energy outer transition $|\uparrow\rangle_\vartheta \rightarrow |\uparrow\downarrow\Uparrow\rangle_\vartheta$ ($|\uparrow\rangle_x \rightarrow |\uparrow\downarrow\Uparrow\rangle_x$). The incident polarisation and power of the resonant continuous-wave (CW) laser is set using a combination of a motorised polariser, half- and quarter-waveplates (QWPs). In both magnetic field configurations the resonant CW laser is set to be fully co-polarised with the driven transition, whereas the pulsed laser was set to be circularly polarised. In the oblique configuration the pulses are set to be cross-polarised with respect to the Λ-system we are working on. To minimise the effect of the CW resonant laser during the coherent control experiment while maintaining high enough detected photon counts, we set its power in the range of $50-150$ nW which is $\sim$25 times lower than the value where we can distinguish any observable dressing of the transition (see Supplementary material). Residual back-reflected laser light from the resonant CW laser, is rejected by spectral filtering in the spectrometer. For readout we isolate spontaneously emitted photons from the $|\uparrow\downarrow\Uparrow\rangle_\vartheta \rightarrow |\downarrow\rangle_\vartheta$ ($|\uparrow\downarrow\Uparrow\rangle_x \rightarrow |\downarrow\rangle_x$) transition in the oblique (Voigt) configuration (bottom of figure 1(a)) by spectral filtering through a double 1 m long custom-built spectrometer with intermediate slits that has $\sim$50% efficiency at maximum resolution ($\sim 8.5\,\mu$eV), while photon detection is performed using a single photon counting module with $\sim 150\,\mathrm{s}^{-1}$ dark counts at the output of the spectrometer. The location of the pulses with respect to the PL spectrum of the charged QD in the oblique field configuration is shown in figure 1(b), where the shaded areas on the highest energy transitions highlight the resonantly driven (grey) and detected (orange) transitions.

2.3. Zeeman splitting interaction & influence on the selection rules

We address a singly charged InAs QD hosting a resident electron spin in the ground state and a trion in the excited state. The magnetic field dependence of the optical transition energies between the trion and ground-spin state manifolds reflects the interplay of the linear in-field Zeeman interaction and the quadratic diamagnetic shift (see Supplementary material), since the reported Zeeman splittings below, are obtained after subtracting the common quadratic diamagnetic shift γB^2, extracted from a simultaneous fit to the four magneto-photoluminescence transition energies. The extracted values for the oblique and the Voigt configurations are $\gamma_\vartheta = 6.02\,\mu\mathrm{eV/T}^2$ and $\gamma_x = 4.40\,\mu\mathrm{eV/T}^2$, from which we get the value for the Faraday configuration $\gamma_z = 10.90\,\mu\mathrm{eV/T}^2$. We investigate two magnetic field configurations, with the applied magnetic field lying in the x–z plane, at angles $\vartheta = 60°(90°)$ with respect to the growth axis $\hat{z}$, corresponding to the oblique (Voigt) geometry. Electron and heavy-hole Zeeman interactions are described by effective spin-1/2 Hamiltonians with different in-plane and out-of-plane g-factors. The oblique magnetic field mixes the z-basis spins and generates unequal superpositions for the ground spin- and excited trion- states which we label as $|\uparrow\rangle_\vartheta$, $|\downarrow\rangle_\vartheta$, and $|\uparrow\downarrow\Uparrow\rangle_\vartheta$, $|\uparrow\downarrow\Downarrow\rangle_\vartheta$. The composition of these states in terms of the z-basis spins is directly related to the magnetic field angle and the in-plane ($\mathrm{g}^x_{\mathrm{e/h}}$) and out-of-plane ($\mathrm{g}^z_{\mathrm{e/h}}$) g-factors [24]. From the fitted magnetophotoluminescence spectra in figure 2(a) taken in the oblique configuration, we extract the g-factors $\mathrm{g}^\vartheta_{\mathrm{e}} = 0.46$ and $\mathrm{g}^\vartheta_{\mathrm{h}} = 0.92$. Combining this with the magnetophotoluminescence spectra in the Voigt configuration in figure 2(b), we extract both the in-plane and out-of-plane g-factors for the electron and the heavy-hole. The electron is found to be only weakly anisotropic since $\mathrm{g}^z_{\mathrm{e}} = 0.50$ and $\mathrm{g}^x_{\mathrm{e}} = 0.45$, whereas the hole g-factor has a more pronounced anisotropy with $\mathrm{g}^z_{\mathrm{h}} = 1.82$ and $\mathrm{g}^x_{\mathrm{h}} = 0.13$. This anisotropy is particularly important in the oblique-field geometry, where the in-plane component of the magnetic field induces heavy-hole mixing, thereby renormalising the hole response and modifying the optical selection rules. Because the electron g-factor is only weakly anisotropic, the effective Zeeman field remains nearly collinear with the applied magnetic field. By contrast, the strong anisotropy of the heavy-hole primarily affects the trion eigenstates, setting their Zeeman splitting and, crucially, determining the optical coupling strengths and transition polarisations of the oblique-field double-Λ system. The four allowed optical transitions arise from the coupling between the two ground-state electron eigenstates and the two excited-state trion eigenstates and inherit

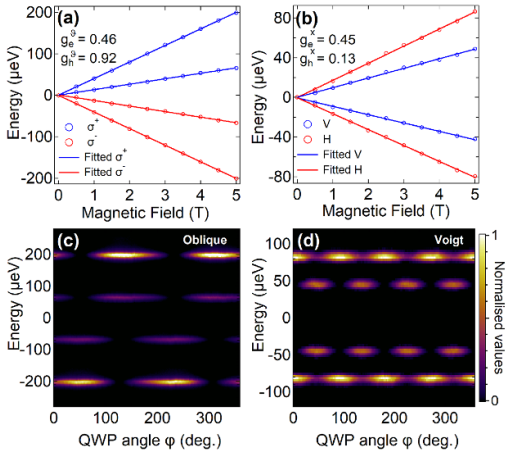


Figure 2. Zeeman splitting in the oblique (a) and in the Voigt (b) configurations. Polarisation analysis of the four emission transitions at 5 T is shown for the oblique (c) and Voigt (d) configurations. In oblique field geometry the two higher energy transitions are σ^+ polarised whereas the two lower energy transitions σ^-. (d) In Voigt geometry, the outer transitions become horizontally polarised while the inner transitions vertically polarised. Figures (c) and (d) share the same colourscale.

their polarisation properties from the optical selection rules in the applied magnetic field. More generally, the oblique-field selection rules differ from the purely circular Faraday limit and the purely linear Voigt limit, and are sensitive to the underlying spin mixing [24]. At 5T, spectrally- and polarisation-resolved photoluminescence is used to determine the optical coupling strengths and transition polarisations for each magnetic field orientation, using rotating QWP polarimetry. The PL is sent through a rotating QWP followed by a fixed horizontal polariser, and the transmitted spectra are quoted as a function of the QWP angle φ. Using Fourier analysis for the spectrally integrated signal of each transition we extract the polarisation properties. In the oblique configuration we find that all transitions have a high degree of circular polarisation with ($\geqslant$90%) circularity, strongly influenced by the large hole anisotropy (figure 2(c)), and that the two Λ-systems are orthogonally polarised. By contrast, in the Voigt configuration the four transitions are found to be linearly polarised, with the inner transitions being vertically- and the outer horizontally polarised (figure 2(d)). For the complete analysis see Supplementary material.

3. Results

3.1. Rabi oscillations

Coherent single-qubit rotations are evidenced by Rabi oscillations under non-resonant pulsed driving, an approach widely used in QD spin-qubit control experiments [3–15]. In both magnetic field orientations, the qubit is encoded in the ground state electron spin of a negatively charged QD, while far red-detuned picosecond (ps) pulses couple these ground states to the trion manifold only virtually [34]. Because the trion is negligibly populated during the pulse, the interaction can be described as an effective AC-Stark coupling, which induces a coherent mixing of the spin states together with an additional AC-Stark phase [34]. As a result, the pulse implements a spin rotation by an angle that scales approximately as the square root of the pulse power, $\theta \propto \sqrt{P}$. The key difference between the two magnetic field configurations investigated here, lies in the orientation of the axis about which the spin qubit rotates. In the oblique-field configuration, we label the ground states, as $|\uparrow\rangle_\vartheta$ and $|\downarrow\rangle_\vartheta$. On the Bloch sphere, a single red-detuned circularly polarised picosecond pulse, cross-polarised with respect to the relevant Λ-system, drives rotations about a tilted axis $\hat{n}$, whose orientation is determined by the angle of the applied magnetic field, assuming weak electron g-factor anisotropy (Inset figure 3(a)). By contrast, in Voigt geometry, the ground states are $|\uparrow\rangle_x$ and $|\downarrow\rangle_x$, so the Bloch vector rotates about the $\hat{x}$ axis defined by the magnetic field, which is perpendicular to the growth axis $\hat{z}$ (Inset figure 3(b)). In addition, the Bloch sphere representation used throughout this work is fully equivalent to the density-matrix description, with the South (North) pole corresponding to the pure state $\rho = |\uparrow\rangle\langle\uparrow|$ ($\rho = |\downarrow\rangle\langle\downarrow|$). For both magnetic field orientations we therefore observe that for increasing pulse powers the detected signal shows a clear oscillatory behaviour with damping, indicating effective Rabi rotations of the qubit about the respective rotations axes.

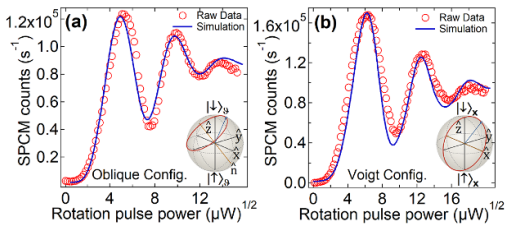


Figure 3. (a) Rabi oscillations in oblique configuration as a function of pulse power. Experimental data are shown as red markers and the corresponding simulation is shown as a blue solid line. Inset: Bloch Sphere representation of the driven Bloch-vector as it is rotated about the axis $\hat{n}$, tilted by 60° deg. (b) Rabi oscillations in Voigt configuration. Inset: Bloch Sphere representation at a field angle of 90°, where the Bloch vector is rotated about the $\hat{x}$ axis.

The resulting signal for the oblique (Voigt) configuration, collected from the $|\uparrow\downarrow\Uparrow\rangle_\vartheta \rightarrow |\downarrow\rangle_\vartheta$ ($|\uparrow\downarrow\Uparrow\rangle_x \rightarrow |\downarrow\rangle_x$) transitions, is plotted in (figures 3(a) and (b)) as a function of the $\sqrt{P}$ of the non-resonant pulses. The damping observed in both geometries is consistent with a combination of excitation-induced dephasing, phonon-assisted relaxation, spontaneous emission, and Larmor precession [22]. To quantify these effects, we compare the measurements with master-equation simulations of the driven four-level system implemented in QuTiP [35, 36]. The model includes spontaneous emission, pure dephasing, and excitation-induced dephasing arising from coupling to longitudinal acoustic phonons, which produces pulse-area-dependent Rabi oscillation damping in InAs/GaAs QDs [22]. The parameters extracted from these fits are then used consistently in the simulations of the Rabi oscillations, Ramsey interference, and general SU(2) control.

3.2. Ramsey interference

Following the demonstration of Rabi oscillations, we probe the ground-state coherence using a Ramsey sequence. In both geometries, the sequence consists of two identical control pulses separated by a variable delay τ, with each pulse chosen to implement an effective $\pi/2$ rotation that brings the Bloch vector to the equator. The key distinction is that, in the oblique-field configuration, where the magnetic field is oriented at $\vartheta = 60°$ with respect to the growth axis, this effective $\pi/2$ operation requires an actual pulse rotation angle of approximately $\theta \approx 109°$ (considering instantaneous pulse rotations). By contrast, in the Voigt geometry, where the magnetic field is oriented at $\vartheta = 90°$, the effective $\pi/2$ condition coincides with the physical $\pi/2$ pulse ($\theta = 90°$). The Rabi oscillation data allow us to identify and calibrate the pulse powers that correspond to these operating points. We therefore use two identical effective $\pi/2$ pulses in the oblique-field Ramsey experiment and two identical $\pi/2$ pulses in the Voigt case. In the oblique-field configuration, the first pulse rotates the Bloch vector from the north pole to the equatorial plane about the fixed control axis $\hat{n}$, thus preparing a coherent superposition of $|\uparrow\rangle_\vartheta$ and $|\downarrow\rangle_\vartheta$ (inset of figure 4(a)). During the free-evolution interval, the spin precesses about the $\hat{z}$ axis, at the Larmor frequency $\omega^{\mathrm{L}}_\vartheta/2\pi = 31.75\,\mathrm{GHz}$, leading to an overall rotation by an angle $\phi = \omega\tau$ [5–11, 15]. The second pulse then performs a further rotation about the same control axis $\hat{n}$, mapping the position on the equator into a delay-dependent ground-state superposition. As in the Rabi-oscillation measurements, the final population is read out through spontaneous spectrally filtered emission on the $|\uparrow\downarrow\Uparrow\rangle_\vartheta \rightarrow |\downarrow\rangle_\vartheta$ transition, yielding Ramsey fringes as a function of τ (figure 4(a)). In this representation, the maximum signal corresponds to a superposition near the $|\uparrow\rangle_\vartheta$ state, while the minimum signal corresponds to a superposition near the $|\downarrow\rangle_\vartheta$ as illustrated in the inset of figure 4(a). The corresponding Ramsey measurement in Voigt geometry follows the same general protocol, but with control pulses implementing $\pi/2$ rotations, creating coherent superpositions between $|\uparrow\rangle_x \leftrightarrow |\downarrow\rangle_x$, consistent with the different orientation of the rotation axis in that configuration (figure 4(b)). The Larmor frequency here is $\omega^{\mathrm{L}}_x/2\pi = 30.9\,\mathrm{GHz}$, consistent with the slightly smaller electron ground state splitting. The measured fringes are well reproduced by our master-equation model using the parameters extracted from the Rabi-oscillation analysis. The delay τ is controlled with a Mach–Zehnder interferometer [37, 38] in the pulsed-excitation path, where a motorised translation stage provides coarse delay steps of 1.33 ps, spanning delays from $\tau = 0$ up to 1 ns.

An interesting difference between the two configurations is the initial phase offset $\Delta\phi$ of the Ramsey fringes (here $\Delta\phi \cong 0.24\,\mathrm{rad}$). Neglecting Larmor precession during the all-optical rotations, in the Voigt configuration, two successive $\pi/2$ pulses bring the Bloch vector from the north pole to the south pole of the Bloch sphere, yielding maximum counts and therefore a zero Ramsey-fringe phase. In the oblique

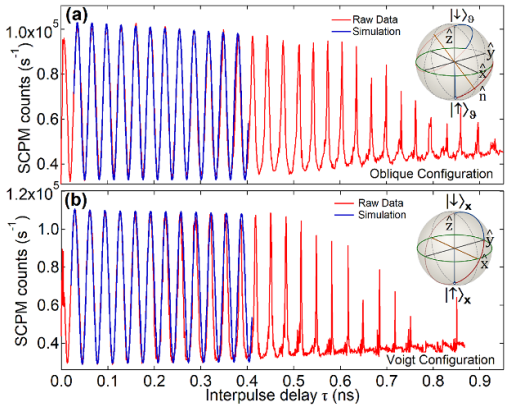


Figure 4. Ramsey interference measured by driving the qubit with two effective rotations that bring the Bloch vector to the equator, separated by an interpulse delay in the oblique (a) and Voigt (b) configurations. The red solid line denotes the experimental data and the solid blue line is our modelled Ramsey interference. At zero delay the noise is because of optical interference between the pulses. At larger delays, signatures consistent with nuclear-spin polarisation become clearly visible. The insets show a simplified state trajectory for two pulses with optical area of two $\pi/2$ in the Voigt and pulses corresponding to $\theta = 109^\circ$ in the oblique configuration, at a delay, for which the second pulse brings the Bloch vector to the opposite spin state.

configuration, the effective $\pi/2$ pulses rotate the Bloch vector about the tilted control axis $\hat{n}$. When applied with zero interpulse delay, these pulses drive a Rabi-like trajectory about $\hat{n}$ (Inset of figure 3(a)). Consequently, the south pole is reached only for a small delay between the pulses, which introduces a finite phase shift in the Ramsey fringes. This phase offset is therefore a direct consequence of the tilted control axis $\hat{n}$.

At longer delays, deviations from simple oscillatory behaviour appear in the form of pronounced spikes in the signal, consistent with signatures of dynamic nuclear-spin polarisation reported previously [39–42]. Interestingly, the onset of this behaviour seems to happen for shorter delays in the Voigt configuration. Strategies to mitigate nuclear-spin and charge-noise limitations, and thereby extend spin coherence in self-assembled QDs, have been extensively explored elsewhere [43].

3.3. Complete coherent control

As a final step, we demonstrate complete coherent control in an oblique magnetic field, namely universal single-qubit operations on the ground $|\uparrow\rangle_\vartheta \leftrightarrow |\downarrow\rangle_\vartheta$ manifold. The protocol generalises the Ramsey sequence using two identical control pulses of equal tunable pulse areas and tunable delays. In this setting, the first pulse applies a coherent rotation about the control axis $\hat{n}$, while Larmor precession during the interpulse delay τ rotates the qubit by an angle $\phi = \omega\tau$ about the $\hat{z}$ axis. The second pulse then induces a further rotation about the axis $\hat{n}$. Two rotations about the fixed control axis $\hat{n}$, separated by an additional controlled rotation about the $\hat{z}$ axis, are sufficient to reach any point on the Bloch sphere, and therefore implement arbitrary SU(2) single-qubit rotations. The experiment is performed at a non-zero pulse delay ($\tau \approx 20 - 140$ ps) to avoid optical-field interference between the two pulses. As in the previous experiments, for each pulse power, which sets the rotation angle, we scan the delay τ and record time-integrated photon counts from the $|\uparrow\downarrow\Uparrow\rangle_\vartheta \rightarrow |\downarrow\rangle_\vartheta$ transition. The resulting data form a two-dimensional control map with axes given by $\sqrt{P}$ and delay τ. The measured map exhibits the characteristic multi-lobed structure expected for coherent SU(2) control in detuned Λ-systems [5, 8, 9, 15] (figure 5(a)). However, in the present case, the multi-lobe pattern also displays distinctive features, including tilted and 'interconnected' lobes. A master-equation model, using parameters independently constrained by the Rabi and Ramsey measurements, reproduces well the observed lobe pattern (figure 5(b)). Finally, we follow a similar procedure to reproduce the complete coherent control of the $|\uparrow\rangle_x \leftrightarrow |\downarrow\rangle_x$ manifold in the Voigt configuration, as indicated in figure 5(c) and its modelled results in figure 5(d). Unlike the Voigt configuration, the oblique-field configuration yields a tilted control axis and asymmetric couplings to the two ground states. Therefore, one would expect that these differences should visibly modify the SU(2) control maps between the two configurations. Interestingly, we show that the SU(2) control maps show minor differences mostly related to the different Larmor frequencies and the slightly modified pulse powers due to asymmetric couplings. Overall, these results establish that self-assembled InAs QDs in a fixed oblique magnetic field support universal all-optical single-qubit control, while preserving the tunability of the spin eigenstates through the field orientation.

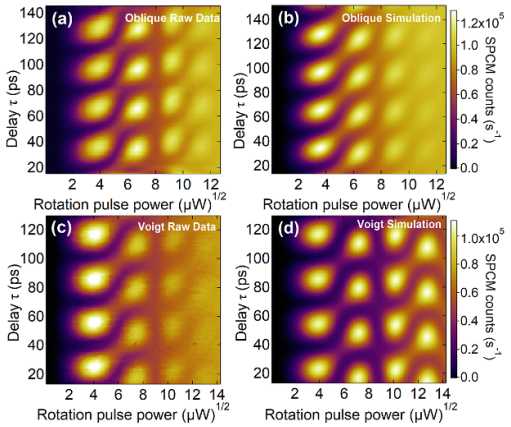


Figure 5. Detected photon counts following excitation with two off-resonant pulses of variable power and variable interpulse delay. Scanning these parameters enables access to the full Bloch Sphere. (a) Experimental data for the oblique configuration, (b) corresponding simulation. (c) Experimental data for the Voigt configuration, and (d) corresponding simulation. The same colourbar is used for (a) and (b), and for (c) and (d).

4. Simulations

We model the QD as a four-level double-Λ system comprising two ground spin states, $|1\rangle$ and $|2\rangle$, split by the ground state splitting $\Delta E_{\rm gs}$, and two excited states, $|3\rangle$ and $|4\rangle$, separated by the excited state splitting $\Delta E_{\rm es}$. The dynamics is governed by a Lindblad master equation:

$$\dot{\rho} = -\mathrm{i}\left[H, \rho\right] + \sum_{m} \mathcal{L}\left(c_m\right), \tag{1}$$

where $\mathcal{L}(c_m)$, the Lindblad superoperators of the collapse operators c_m. All calculations are performed in a frame rotating at the CW laser frequency ω_l, within the rotating-wave approximation. The unperturbed Hamiltonian in this frame is

$$H_0 = \frac{\Delta E_{\rm gs}}{2}\left(p_{22} - p_{11}\right) + \Delta_{\rm cw} p_{33} + \left(\Delta_{\rm cw} + \Delta E_{\rm es}\right) p_{44}, \tag{2}$$

where $p_{ff} = |f\rangle\langle f|$ is the population projection operator onto the states, and $\Delta_{\rm cw}$ is chosen to render the CW laser resonant with the outer $|1\rangle \leftrightarrow |4\rangle$ transition. The Hamiltonian of a CW field of Rabi frequency $\Omega_{\rm cw}$ that drives this transition time-independently in the rotating frame is:

$$H_{\rm cw} = \frac{\Omega_{\rm cw}}{2} k_{14}\left(p_{41} + p_{41}^{\dagger}\right), \tag{3}$$

where k_{14} is the coupling dipole coefficient in each configuration that we extract from (figures 2(c) and (d)). A pulsed field with Gaussian envelope $\Omega(t) = \Omega_p \exp\left[-(t-t_0)^2/2\sigma^2\right]$ is decomposed into parameters that are responsible for the driving of each transition, based on the polarisation in each geometry:

$$\left.\begin{aligned} \Omega_p^{14}(t) &= \Omega_p^{24}(t) = \Omega(t)\cos\alpha, \\ \Omega_p^{13}(t) &= \Omega_p^{23}(t) = \Omega(t)\,\mathrm{e}^{\mathrm{i}\beta}\sin\alpha \end{aligned}\right\} \text{ oblique}$$
$$\left.\begin{aligned} \Omega_p^{14}(t) &= \Omega_p^{23}(t) = \Omega(t)\cos\alpha, \\ \Omega_p^{13}(t) &= \Omega_p^{24}(t) = \Omega(t)\,\mathrm{e}^{\mathrm{i}\beta}\sin\alpha \end{aligned}\right\} \text{ Voigt} \tag{4}$$

where α and β are set to correspond to the polarisation and relative phase, so that the pulses drive the transitions accordingly for each configuration. The pulse carrier is detuned from the CW frame by Δ_p. The full pulse Hamiltonian is

$$H_p(t) = \frac{1}{2}\sum_{i,j} k_{ij}\Omega_p^{ij}(t)\,\mathrm{e}^{-\mathrm{i}\Delta_p t} p_{ij} + \mathrm{H.C} \tag{5}$$

where $i(j)$ are the ground (excited) state indices, k_{ij} the coupling dipole coefficient, and Ω_p^{ij} is the pulse driving term for every transition in each configuration. Radiative decay from each excited state to each ground state is included through collapse operators $c_{ji} = \sqrt{\Gamma_{ji}}\,p_{ji}$ with Γ_{ji}^{-1} the trion lifetime. Pure

dephasing is modelled by static Lindblad operators $\sqrt{\gamma_d}p_{jj}$, representing charge noise, supplemented by a time-dependent phonon term $\sqrt{\alpha_{\text{phonon}}}|\Omega_p(t)|p_{jj}$. Starting from $\rho(0) = |2\rangle\langle 2|$, we compute the time-integrated photon flux on the $|4\rangle \rightarrow |2\rangle$ channel,

$$N = \int \Gamma_{42}\langle p_{44}\rangle \, \mathrm{d}t, \tag{6}$$

as a function of pulse area, using the QuTiP master equation solver. The simulation parameters used for the oblique (Voigt) configuration ($\vartheta = 60°(90°)$) are: $\frac{\Delta E_{\text{gs}}}{2\pi\hbar} = 31.75\,\text{GHz}(30.9\,\text{GHz})$, $\frac{\Delta E_{\text{es}}}{2\pi\hbar} = 63.4\,\text{GHz}(9.7\,\text{GHz})$, extracted from the Zeeman Splitting, $\frac{\sigma}{2\pi} = 98\,\text{GHz}$ which corresponds to a width of ≈ 3 ps pulse, $\frac{\Omega^{\text{CW}}_{\text{Rabi}}}{2\pi} = 1\,\text{GHz}$, $\frac{\Omega^{\text{CW}}_{\text{Ramsey}}}{2\pi} = \frac{\Omega^{\text{CW}}_{\text{Rabi}}}{\sqrt{3}}$, $\frac{\Omega^{\text{CW}}_{\text{SU(2)}}}{2\pi} = \frac{\Omega^{\text{CW}}_{\text{Rabi}}}{2}$, $\frac{\Omega^{\text{Pulsed}}}{2\pi} \in (0, 2550)\,\text{GHz}$, $\frac{\Delta_{\text{Pulsed}}}{2\pi} = -500\,\text{GHz}$, $\Gamma = k_{ij}^2$, $\gamma_{\text{dephasing}} = 1\,\text{ns}^{-1}$ and $\alpha_{\text{phonon}} = 28 \cdot 10^{-6}\,\text{ns}^{-1}$ are chosen correspondingly to match the experimental behaviour, $\alpha = 90°(45°)$ and $\beta = 10°(90°)$ chosen from the polarisation analysis, $k_{14} = k_{23} = \sqrt{0.75}(\sqrt{0.5})$ and $k_{24} = k_{13} = \sqrt{0.25}(\sqrt{0.5})$ the dipole coupling coefficients, estimated from the polarisation analysis.

Acknowledgments

I.S. acknowledges financial support from the EPSRC Doctoral Training Partnership under grant no. EP/W524670/1. K.B. acknowledges financial support from the EPSRC Doctoral Training Program under grant no. EP/R513349/1. C.S. is grateful for financial support by the BMFTR within the project COMPHORT (16KIS2107). Comphort is funded within the QuantERA program.

Data availability statement

The data that support the findings of this study are not publicly available because the underlying experimental datasets include extensive raw data, calibration files and associated laboratory-specific metadata that have not been curated for public deposition. The data required to support the findings of this study are available from the authors upon reasonable request.

Supplementary Material available at https://doi.org/10.1088/2058-9565/aea92e/data1.

Disclosures

The authors declare no conflicts of interest

ORCID iDs

I Samaras 0009-0000-9903-1373
K Barr 0000-0001-6141-4424
C Schneider 0000-0002-2268-471X
S Höfling 0000-0003-0034-4682
K G Lagoudakis 0000-0002-4410-4755

References

[1] Ramsay A J, Boyle S J, Kolodka R S, Oliveira J B B, Skiba-Szymanska J, Liu H Y, Hopkinson M, Fox A M and Skolnick M S 2008 Fast optical preparation, control and readout of a single quantum dot spin *Phys. Rev. Lett.* **100** 197401
[2] Gerardot B D *et al* 2008 Optical pumping of a single hole spin in a quantum dot *Nature* **451** 441
[3] Mikkelsen M H, Berezovsky J, Stoltz N G, Coldren L A and Awschalom D D 2007 Optically detected coherent spin dynamics of a single electron in a quantum dot *Nat. Phys.* **3** 770
[4] Berezovsky J, Mikkelsen M H, Stoltz N G, Coldren L A and Awschalom D D 2008 Picosecond coherent optical manipulation of a single electron spin in a quantum dot *Science* **320** 349
[5] Press D, Ladd T D, Zhang B and Yamamoto Y 2008 Complete quantum control of a single quantum dot spin using ultrafast optical pulses *Nature* **456** 218
[6] Kim E D, Truex K, Xu X, Sun B, Steel D G, Bracker A S, Gammon D and Sham L J 2010 Fast spin rotations by optically controlled geometric phases in a charge-tunable InAs quantum dot *Phys. Rev. Lett.* **104** 167401
[7] Gupta J A, Knobel R, Samarth N and Awschalom D D 2001 Ultrafast manipulation of electron spin coherence *Science* **292** 2458

[8] De Greve K *et al* 2011 Ultrafast coherent control and suppressed nuclear feedback of a single quantum dot hole qubit *Nat. Phys.* **7** 872
[9] Greve K D, Press D, McMahon P L and Yamamoto Y 2013 Ultrafast optical control of individual quantum dot spin qubits *Rep. Prog. Phys.* **76** 092501
[10] Godden T M *et al* 2012 Coherent optical control of the spin of a single hole in an InAs / GaAs quantum dot *Phys. Rev. Lett.* **108** 017402
[11] Hogg M R and Warburton R J *et al* 2025 Fast optical control of a coherent hole spin in a microcavity *Nat. Phys.* **21** 1475
[12] Koong Z X *et al* 2026 Coherent control of quantum-dot spins with cyclic optical transitions *Nat. Commun.* **17** 7917
[13] Gao W B, Imamoglu A, Bernien H and Hanson R 2015 Coherent manipulation, measurement and entanglement of individual solid-state spins using optical fields *Nat. Photon.* **9** 363
[14] Ding D *et al* 2019 Coherent optical control of a quantum-dot spin-qubit in a waveguide-based spin-photon interface *Phys. Rev. Appl.* **11** 031002
[15] Dusanowski Ł, Nawrath C, Portalupi S L, Jetter M, Huber T, Klembt S, Michler P and Höfling S 2022 Optical charge injection and coherent control of a quantum-dot spin-qubit emitting at telecom wavelengths *Nat. Commun.* **13** 748
[16] Press D *et al* 2010 Ultrafast optical spin echo in a single quantum dot *Nat. Photon.* **4** 367
[17] Yilmaz S T, Fallahi P and Imamoğlu A 2010 Quantum-dot-spin single-photon interface *Phys. Rev. Lett.* **105** 033601
[18] Appel M H *et al* 2021 Coherent spin-photon interface with waveguide induced cycling transitions *Phys. Rev. Lett.* **126** 013602
[19] De Greve K *et al* 2012 Quantum-dot spin–photon entanglement via frequency downconversion to telecom wavelength *Nature* **491** 421
[20] Gao W B, Fallahi P, Togan E, Miguel-Sanchez J and Imamoglu A 2012 Observation of entanglement between a quantum dot spin and a single photon *Nature* **491** 426
[21] Atatüre M, Dreiser J, Badolato A and Imamoglu A 2007 Observation of Faraday rotation from a single confined spin *Nat. Phys.* **3** 101
[22] Ramsay A J, Godden T M, Boyle S J, Gauger E M, Nazir A, Lovett B W, Gopal A V, Fox A M and Skolnick M S 2011 Effect of detuning on the phonon induced dephasing of optically driven InGaAs/GaAs quantum dots *J. Appl. Phys.* **109** 102415
[23] Crooker S A, Brandt J, Sandfort C, Greilich A, Yakovlev D R, Reuter D, Wieck A D and Bayer M 2010 Spin noise of electrons and holes in self-assembled quantum dots *Phys. Rev. Lett.* **104** 036601
[24] Barr K, Hourahine B, Schneider C, Höfling S and Lagoudakis K G 2024 Towards spin state tailoring of charged excitons in InGaAs quantum dots using oblique magnetic fields *Phys. Rev. B* **109** 075433
[25] Poem E, Shemesh J, Marderfeld I, Galushko D, Akopian N, Gershoni D, Gerardot B D, Badolato A and Petroff P M 2007 Polarization sensitive spectroscopy of charged quantum dots *Phys. Rev. B* **76** 235304
[26] Schwan A, Meiners B-M, Greilich A, Yakovlev D R, Bayer M, Maia A D B, Quivy A A and Henriques A B 2011 Anisotropy of electron and hole g -factors in (In,Ga)As quantum dots *Appl. Phys. Lett.* **99** 221914
[27] Hapke-Wurst I, Zeitler U, Haug R and Pierz K 2002 Mapping the g factor anisotropy of InAs self-assembled quantum dots *Physica E: Low Dimens. Syst. Nanostruct.* **12** 802
[28] Belykh V V, Greilich A, Yakovlev D R, Yacob M, Reithmaier J P, Benyoucef M and Bayer M 2015 Electron and hole g factors in InAs/InAlGaAs self-assembled quantum dots emitting at telecom wavelengths *Phys. Rev. B* **92** 165307
[29] Van Hattem B, Corfdir P, Brereton P, Pearce P, Graham A, Stanley M, Hugues M, Hopkinson M and Phillips R 2013 Photoluminescence in tilted magnetic field of triply negatively charged excitons hybridized with a continuum *Acta Phys. Pol. A* **124** 798
[30] Neumann M, Kappe F, Bracht T K, Cosacchi M, Seidelmann T, Axt V M, Weihs G and Reiter D E 2021 Optical stark shift to control the dark exciton occupation of a quantum dot in a tilted magnetic field *Phys. Rev. B* **104** 075428
[31] Jiménez-Orjuela C A, Vinck-Posada H and Villas-Bôas J M 2017 Dark excitons in a quantum-dot–cavity system under a tilted magnetic field *Phys. Rev. B* **96** 125303
[32] Maier S, Gold P, Forchel A, Gregersen N, Mørk J, Höfling S, Schneider C and Kamp M 2014 Bright single photon source based on self-aligned quantum dot–cavity systems *Opt. Express* **22** 8136
[33] Barr K, Cookson T and Lagoudakis K G 2021 Operation of a continuous flow liquid helium magnetic microscopy cryostat as a closed cycle system *Rev. Sci. Instrum.* **92** 123701
[34] Wilkinson T A, Cottrill D J, Cramlet J M, Maurer C E, Flood C J, Bracker A S, Yakes M, Gammon D and Flagg E B 2019 Spin-selective AC stark shifts in a charged quantum dot *Appl. Phys. Lett.* **114** 133104
[35] Johansson J, Nation P and Nori F 2012 QuTiP: an open-source python framework for the dynamics of open quantum systems *Comput. Phys. Commun.* **183** 1760
[36] Johansson J, Nation P and Nori F 2013 QuTiP 2: a python framework for the dynamics of open quantum systems *Comput. Phys. Commun.* **184** 1234
[37] Okada T, Komori K, Goshima K, Yamauchi S, Morohashi I, Sugaya T, Ogura M and Tsurumachi N 2008 Development of high resolution michelson interferometer for stable phase-locked ultrashort pulse pair generation *Rev. Sci. Instrum.* **79** 103101
[38] Barcan R A, Samaras I, Barr K, Juska G, Pelucchi E and Lagoudakis K G 2026 Trion quantum coherence in site-controlled pyramidal InGaAs quantum dots *Sci. Rep.* **16** 4114
[39] Kotur M, Bazhin P S, Kavokin K V, Kopteva N E, Yakovlev D R, Kudlacik D and Bayer M 2026 Dynamic polarization of nuclear spins by optically oriented electrons and holes in lead halide perovskite semiconductors *Phys. Rev. B* **113** 085204
[40] Economou S E and Barnes E 2014 Theory of dynamic nuclear polarization and feedback in quantum dots *Phys. Rev. B* **89** 165301
[41] Yamamoto S, Kaji R, Sasakura H and Adachi S 2025 Effect of oblique magnetic field on dynamic nuclear polarization in single self-assembled quantum dots governed by nuclear quadrupole interaction *Phys. Status Solidi b* **262** 2400535
[42] Ladd T D, Press D, De Greve K, McMahon P L, Friess B, Schneider C, Kamp M, Höfling S, Forchel A and Yamamoto Y 2010 Pulsed nuclear pumping and spin diffusion in a single charged quantum dot *Phys. Rev. Lett.* **105** 107401
[43] Millington-Hotze P, Dyte H E, Manna S, Covre da Silva S F, Rastelli A and Chekhovich E A 2024 Approaching a fully-polarized state of nuclear spins in a solid *Nat. Commun.* **15** 985

Complete coherent control of spin qubits in self-assembled InAs quantum dots under oblique magnetic fields: Supplementary Material

I. P. Samaras,[1] K. Barr,[1] C. Schneider,[2] S. Höfling,[3] and K.G. Lagoudakis[1]

[1] *University of Strathclyde, Glasgow G4 0NG, United Kingdom*
[2] *Institut für Physik, Fakultät V, Carl von Ossietzky Universität Oldenburg, 26129 Oldenburg, Germany*
[3] *Julius-Maximilians-Universität Würzburg, Technische Physik, 97074 Würzburg, Germany*

Here we present additional measurements and analysis for a self-assembled InAs quantum dot investigated as a spin qubit under both oblique and Voigt magnetic fields. Specifically, we report measurements of the Zeeman splitting and diamagnetic shift, together with the spin-qubit eigenstate composition as a function of magnetic-field angle. We provide the detailed methodology used for the full polarisation analysis of all four optical transitions in both oblique and Voigt field configurations. In addition, we describe the experimental approach used for the coherent-control measurements and characterise the power dependence of the resonant initialisation/readout laser, identifying the operating regime relative to the onset of strong driving and dressed-state formation. Finally, we present signatures of nuclear-spin polarisation and examine their dependence on the detuning of the resonant laser.

A. Qubit composition of the oblique magnetic field

To clarify the spin qubit behaviour in an oblique magnetic field, it is useful to recall the treatment of Barr et al. [1]. An oblique field combines an out-of-plane and an in-plane component, parametrised by the tilt angle ϑ measured from the growth axis, such that $\vartheta = 0°$ recovers the pure Faraday configuration and $\vartheta = 90°$ the pure Voigt configuration. The electron Zeeman interaction under such a field takes the form of an effective two-level Hamiltonian in the $\{|\uparrow\rangle_z, |\downarrow\rangle_z\}$ basis,

$$\hat{H}_e(\vartheta) = -\mu_B B \left(g_e^z \cos\vartheta \, \hat{S}_z + g_e^x \sin\vartheta \, \hat{S}_x \right), \qquad (1)$$

whose diagonalisation yields ground-state eigenstates that are unequal superpositions of the $|\uparrow\rangle_z, |\downarrow\rangle_z$ basis states,

$$\begin{aligned} |\uparrow\rangle_\vartheta &= C_2(\vartheta)\,|\downarrow\rangle_z + C_1(\vartheta)\,|\uparrow\rangle_z, \\ |\downarrow\rangle_\vartheta &= C_1(\vartheta)\,|\downarrow\rangle_z - C_2(\vartheta)\,|\uparrow\rangle_z, \end{aligned} \qquad (2)$$

with $C_1(\vartheta)$, $C_2(\vartheta)$ the normalised real superposition weights, as shown in Eq. 3. At $\vartheta = 0°$, $C_1 \to 1$ and $C_2 \to 0$, recovering the pure $|\uparrow\rangle_z$, $|\downarrow\rangle_z$ eigenstates of the Faraday configuration, whereas at $\vartheta = 90°$ the superposition weights become $C_1 = C_2 = 1/\sqrt{2}$, giving the equally weighted superpositions characteristic of the Voigt configuration. At intermediate angles the qubit encoded in the ground-state manifold therefore acquires a continuously tunable, unequal admixture of the two spin projections, meaning that the field angle acts as a knob directly setting the basis-state weighting, as summarized in Figs. S1(a), (b).

B. Zeeman interaction & Diamagnetic shift

Figure S2(a) shows the evolution of the optical transition energies between the ground-spin state manifold and the trion manifold as a function of magnetic field. This dependence arises from the interplay between the Zeeman interaction, which shifts the energies linearly with magnetic field and lifts the spin-state degeneracy, and the diamagnetic shift, which contributes a quadratic-in-field correction to the transition energies. As a result, the measured spectral lines exhibit a characteristic field dependence that cannot be described by a purely linear model alone. By simultaneously fitting the magnetic-field dependence of the four optical transitions, we extract the diamagnetic contribution and obtain a diamagnetic coefficient of $\gamma_\vartheta = 6.02\,\mu\mathrm{eV/T^2}$, as presented in Fig. S2(b). Figures S2 (c), (d) show the Voigt equivalent of Figures S2 (a), (b) correspondingly, where we report a diamagnetic coefficient of $\gamma_x = 4.40\,\mu\mathrm{eV/T^2}$ in the Voigt case. The diamagnetic shift in self-assembled InAs quantum dots is known to depend on the orientation of the applied magnetic field, reflecting the anisotropic spatial confinement of the carrier wavefunctions.

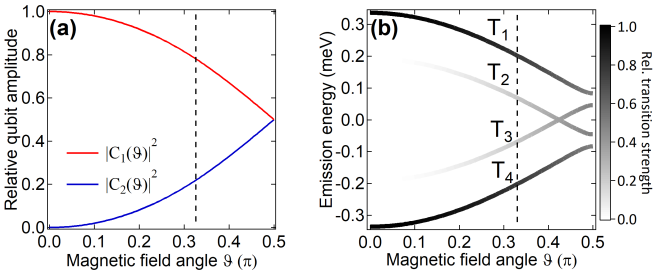


FIG. S1. (a) Squared magnitudes of normalised ground-state basis weights $C_1(\vartheta)$ and $C_2(\vartheta)$ as a function of field angle. An asymmetric spin weight occurs between the two ground states when $\vartheta < 90°$. The vertical dashed line depicts the position of the 60° configuration. (b) Modeled four-level splitting (T_1–T_4) of the QD, studied in the manuscript, versus magnetic field angle ($B_0 = 5$ T). The lines depict the transition energies and their colour indicates their transition intensities according to the colour scale. At 60° the ratio of the relative transition strength is $\sim 0.75 : 0.25$.

$$C_1(\vartheta) = \frac{1}{N_e(\vartheta)}\left[g_e^z\cos\vartheta + \sqrt{(g_e^z\cos\vartheta)^2 + (g_e^x\sin\vartheta)^2}\right], \quad C_2(\vartheta) = \frac{g_e^x\sin\vartheta}{N_e(\vartheta)},$$
$$N_e(\vartheta) = \sqrt{2\left[(g_e^z\cos\vartheta)^2 + (g_e^x\sin\vartheta)^2 + g_e^z\cos\vartheta\sqrt{(g_e^z\cos\vartheta)^2 + (g_e^x\sin\vartheta)^2}\right]} \tag{3}$$

More generally, the diamagnetic response is related to the spatial extent and localisation of the exciton wavefunction, as discussed by Nash et al. [2]. Van Hattem et al. [3] measured this angular dependence for neutral and charged excitons, including X^-, while Van Bree et al. [4] described the angular variation using $\gamma(\vartheta) = \gamma_z\cos^2\vartheta + \gamma_x\sin^2\vartheta$, where ϑ is measured from the Faraday geometry. Using the experimentally determined values $\gamma_\vartheta \equiv \gamma(60°) = 6.02\ \mu\text{eV/T}^2$ and $\gamma_x \equiv \gamma(90°) = 4.40\ \mu\text{eV/T}^2$, this relation gives a Faraday diamagnetic shift coefficient of $\gamma_z \equiv \gamma(0°) \approx 10.90\ \mu\text{eV/T}^2$.

C. polarisation analysis using the rotating QWP polarimetry.

The polarisation states of the four optical transitions were determined using rotating quarter-wave-plate polarimetry for both the oblique and Voigt magnetic-field orientations. The emission was passed through a rotating quarter-wave plate followed by a fixed linear polarisation analyser, as shown in Fig S3. For each field orientation, the emission spectrum was recorded as a function of the wave-plate angle φ from 0° to 358° in 2° increments. At each angle, the spectrum was fitted simultaneously with four Lorentzian lines corresponding to the four transitions, and the area of each fitted Lorentzian was taken as the corresponding transition intensity I(φ).

Because the rotating-quarter-wave-plate signal is 180° periodic, the two non-overlapping intervals $0° \le \varphi \le 178°$ and $180° \le \varphi \le 358°$ each contain one complete period. Each interval contains $N = 90$ equally spaced points and was analysed independently. For either interval, with φ_j denoting the sampled wave-plate angles and $I(\varphi_j)$ the Lorentzian area extracted for a given transition, the Fourier coefficients were calculated directly as

$$A = \frac{2}{N}\sum_{j=0}^{N-1} I(\varphi_j),$$
$$B = \frac{4}{N}\sum_{j=0}^{N-1} I(\varphi_j)\sin(2\varphi_j),$$
$$C = \frac{4}{N}\sum_{j=0}^{N-1} I(\varphi_j)\cos(4\varphi_j), \tag{4}$$
$$D = \frac{4}{N}\sum_{j=0}^{N-1} I(\varphi_j)\sin(4\varphi_j)$$

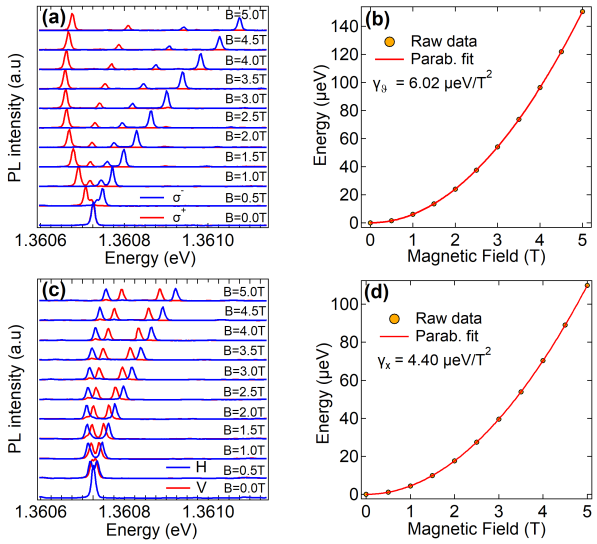


FIG. S2. (a) Raw photoluminescence spectra recorded at different magnetic-fields strengths B in the oblique geometry. (b) Quadratic field dependence of the transition energies attributed to the diamagnetic shift (fit). (c) PL spectra for increasing magnetic field in Voigt. (d) Diamagnetic shift fit in the Voigt geometry.

The angular arguments are expressed in radians when evaluating the trigonometric functions. With this normalisation, the corresponding angular intensity dependence is:

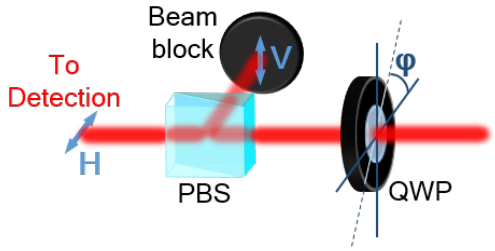


FIG. S3. Rotating quarter-wave-plate polarimetry setup. Photoluminescence from the QDs passes through a rotating quarter-waveplate (QWP) followed by a polarising beamsplitter that acts like a fixed, horizontally polarised linear polariser. The angle $\varphi = 0°$ corresponds to the fast axis of the waveplate (thin white line on QWP body) being parallel to the transmission polarisation of the PBS (parallel to the optical table).

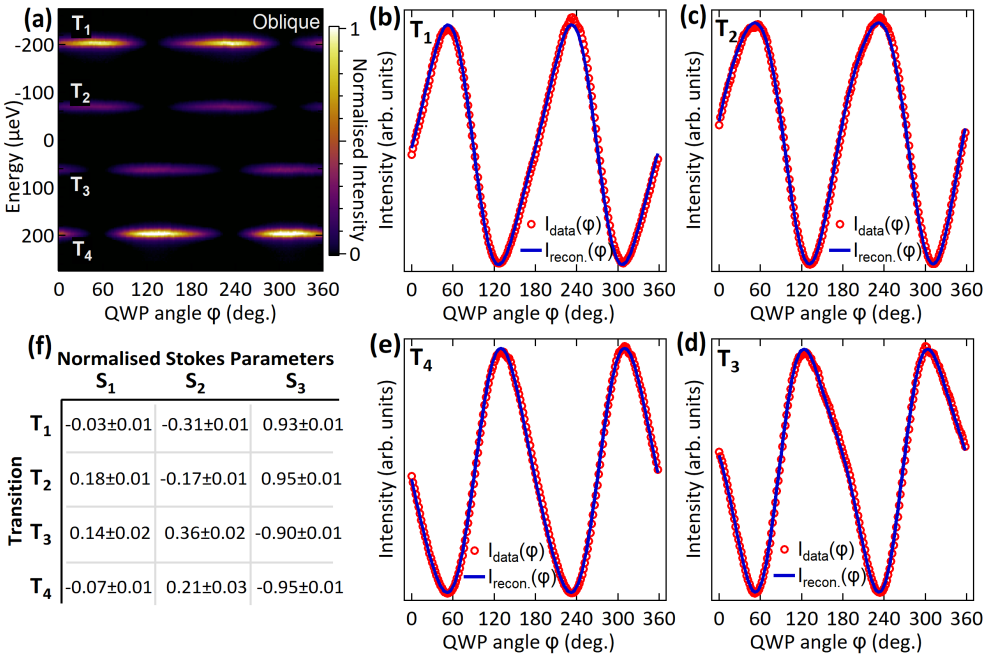


FIG. S4. Rotating quarter-wave-plate polarimetry in the oblique magnetic-field orientation. (a) Quarter-wave-plate-angle-resolved emission spectrum containing the four optical transitions; the boxes highlight the transitions analysed. At each wave-plate angle, the spectrum was fitted simultaneously with four Lorentzian lines. (b–e) Extracted intensity $I_{data}(\varphi)$ of each transition, determined from the area of the corresponding fitted Lorentzian peak. Markers ($I_{data}(\varphi)$) show the extracted experimental values, while the solid curves ($I_{recon.}(\varphi)$) show the angular dependence reconstructed from the Fourier coefficients A, B, C, and D calculated directly from these data. The close agreement between the extracted and reconstructed profiles demonstrates that the Fourier decomposition accurately captures the polarisation dependence of each transition. (f) Compact matrix of the corrected normalised Stokes parameters S_1, S_2, S_3 for the four transitions. For each parameter, the quoted value is the mean obtained from the two non-overlapping 180° periods of the acquisition, and the quoted uncertainty is their sample standard deviation. The degree of polarisation is above 97% for all four transitions.

$$I(\varphi) = \frac{1}{2}[A + Bsin(2\varphi) + Ccos(4\varphi) + Dsin(4\varphi)] \quad (5)$$

Thus, A, B, C, and D are obtained by direct Fourier projection of the Lorentzian peak areas $I(\varphi)$, rather than by fitting the polarisation dependence [5]. Therefore, The Stokes parameters reconstructed from the Fourier coefficients were calculated according to

$$\begin{aligned} s_0 &= A - C, \\ s_1 &= 2C, \\ s_2 &= 2D, \\ s_3 &= B, \end{aligned} \quad (6)$$

The polarisation state was then expressed using the normalised corrected Stokes parameters:

$$\begin{aligned} S_1 &= \frac{s_1}{s_0}, \\ S_2 &= \frac{s_2}{s_0}, \\ S_3 &= \frac{s_3}{s_0}, \end{aligned} \quad (7)$$

S_1 corresponds to linear H/V , S_2 to linear D/A and S_3 to circular σ^+/σ^- polarisation. The degree of polarisation is then calculated according to

$$DOP = \sqrt{S_1^2 + S_2^2 + S_3^2} \quad (8)$$

After having done this analysis, we can quote values and the experimental variation. The complete analysis chain, which includes simultaneous four-Lorentzian spectral fitting, Fourier decomposition, Stokes reconstruction and normalisation, was performed separately for the two non overlapping 180° periods. This yields two determinations, $S_i^{(1)}, S_i^{(2)}$, of each normalised Stokes parameter. the values quoted in the manuscript are their mean,

$$\bar{S}_i = \frac{S_i^{(1)} + S_i^{(2)}}{2} \quad (9)$$

and the quoted uncertainty is their sample standard deviation,

$$\sigma_{S_i} = \sqrt{\frac{(S_i^{(1)} - \bar{S}_i)^2 + (S_i^{(2)} - \bar{S}_i)^2}{2-1}} = \frac{|S_i^{(1)} - S_i^{(2)}|}{\sqrt{2}} \quad (10)$$

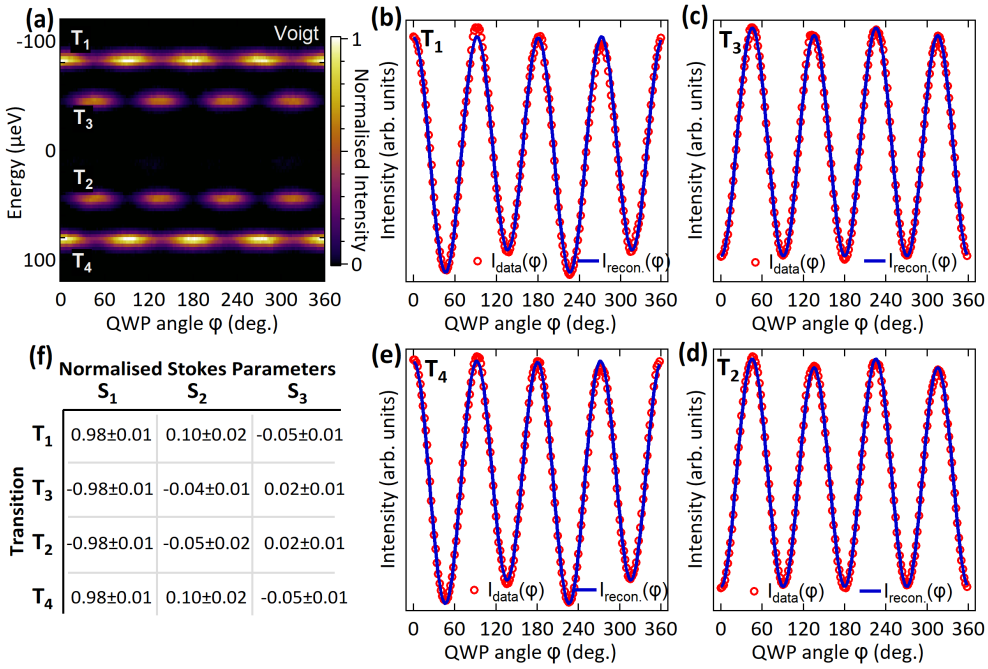


FIG. S5. Rotating quarter-wave-plate polarimetry in the Voigt magnetic-field orientation. (a) Quarter-wave-plate-angle-resolved emission spectrum containing the four optical transitions; the boxes highlight the transitions analysed. At each wave-plate angle, the spectrum was fitted simultaneously with four Lorentzian lines. (b–e) Extracted intensity $I_{data}(\varphi)$ of each transition, determined from the area of the corresponding fitted Lorentzian peak. Markers ($I_{data}(\varphi)$) show the extracted experimental values, while the solid curves ($I_{recon.}(\varphi)$) show the angular dependence reconstructed from the Fourier coefficients A, B, C, and D calculated directly from these data. The close agreement between the extracted and reconstructed profiles demonstrates that the Fourier decomposition accurately captures the polarisation dependence of each transition. (f) Compact matrix of the corrected normalised Stokes parameters S_1, S_2, S_3 for the four transitions. For each parameter, the quoted value is the mean obtained from the two non-overlapping 180° periods of the acquisition, and the quoted uncertainty is their sample standard deviation. The degree of polarisation is above 98% for all four transitions.

The uncertainty therefore quantifies the repeatability of the reconstructed polarisation parameters between the two non-overlapping complete periods of the same angular acquisition. Figure S4 shows the data and reconstruction for the oblique magnetic-field orientation, while Fig. S5 shows the corresponding analysis for the Voigt orientation. In each case, the quarter-wave-plate-angle-resolved emission spectrum is shown with the four optical transitions used in the analysis highlighted. At every wave-plate angle the spectrum was fitted simultaneously with four Lorentzian lines, and the area of each fitted peak was used to construct $I_{data}(\varphi)$ for the corresponding transition. These extracted Lorentzian areas are compared with the signals $I_{recon.}(\varphi)$, reconstructed from the directly calculated Fourier coefficients A, B, C, and D. The close agreement between the extracted angular profiles and the reconstructed signals provides a direct visual check that the Fourier components used in the Stokes reconstruction accurately describe the observed polarisation response. The final panel of each figure summarizes the corrected normalised Stokes parameters for the four transitions.

D. Dual pulse experiment details for complete coherent control

Both the Ramsey interference experiment and the complete coherent control require the generation of dual pulses with controllable interpulse delay τ. To generate such pulse sequences we use a modified Mach-Zehnder interferometer in the mirror-retroreflector configuration as shown in Fig. S6. As the retroreflector is mounted on a motorised linear translation stage, the pulses reflected back from it, experience a time delay that is proportional to the distance of the retroreflector shift. At the output beam splitter the two pulses coming from the variable and fixed delay arms are combined and sent to the sample. One of the critical aspects of the dual pulse experiments is the requirement to have two identical intensity pulses. Minor misalignment or non-ideal splitting ratio of the beam splitters can lead to pulses with different intensities and therefore different rotation angles for each pulse. To eliminate this issue we always compare the effect of the pulses by performing a Rabi rotation experiment for each of the pulses coming from the two delay arms.

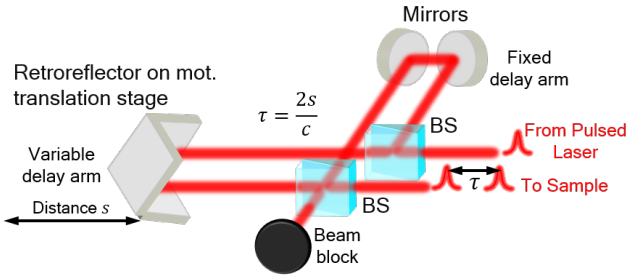


FIG. S6. (a) Schematic diagram of the setup for the generation of dual pulses with variable delays. The retroreflector (RR) is positioned on a motorised translation stage (not shown) that enables the displacement of the RR parallel to the laser beam. The pulse from the fixed arm and the delayed pulse from the RR are combined at the output beam splitter (BS) of the Mach-Zehnder interferometer and are sent to the sample. Both the input and output beam splitters are 50:50 and non-polarising.

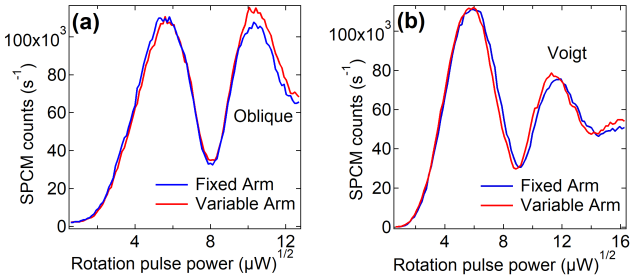


FIG. S7. (a) Rabi rotation measurements performed for each delay arm in the oblique configuration. (b) Corresponding Rabi rotation measurements in the Voigt configuration, shown separately for the two delay arms. For both configurations the individual traces are obtained by selectively blocking one interferometer arm at a time and recording the complete power dependence, allowing the Rabi oscillations associated with each arm to be resolved independently.

Fig. S7(a) shows the two Rabi rotation experiments for each of the pulses for the oblique and the Fig. S7(b) for the Voigt configuration complete coherent control experiments. A good overlap for all powers indicates that the alignment and power balancing are optimal.

E. Dressing of the resonantly driven transition

All coherent control experiments are performed with the resonant initialization/readout laser driving the outer transition of the QD in a continuous manner. To assess the effect of the CW resonant laser and ensure that it is only driving the transition weakly, we perform an additional characterisation whereby we increase the power of the resonant laser while we observe the spectral shape of the diagonal transition of the corresponding Λ system under above band excitation ($\lambda_{Ab.Bd} = 780nm$, $P_{Ab.Bd} = 150nW$). Figure S8(a) presents the PL spectrum from the diagonal transition as a function of the applied CW resonant driving laser power. With increasing CW resonant power, clear signatures of optical dressing (spectral doublet as shown by the level diagram in Fig. S8(b)) emerge only for powers above $\sim 2.5\,\mu$W, indicating the onset of a substantial modification of the transition by the driving field. Because the power range used in the coherent-control experiments lies ~ 25 times below this threshold, we ensure that the CW resonant laser operates in the weak driving regime.

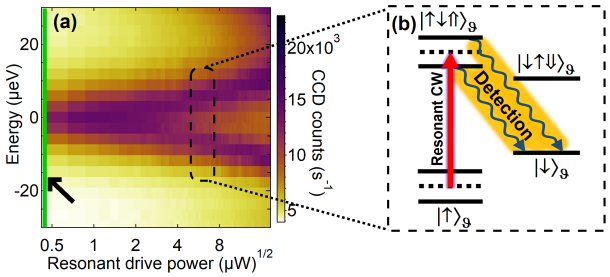


FIG. S8. (a) Raw PL spectra recorded for increasing CW power, with the x-axis displayed in logarithmic scale. At $\sim 2.5\,\mu$W we observe dressed states caused by the CW power. The black arrow indicates the green shaded area where we operate in the coherent control experiment. (b) Double Λ-system at $\sim 6.5\,\mu$W in order for the reader to understand how this phenomenon affect our system.

F. Manifestations of nuclear polarisation effects under oblique magnetic fields

During the acquisition of Rabi-oscillation and Ramsey-interference measurements, we observed that the coherence properties depend reproducibly on the detuning of the resonant continuous-wave (CW) laser from the targeted optical transition. In particular, the form of the Rabi oscillations changes systematically with CW detuning: by adjusting the detuning, the signal can be made

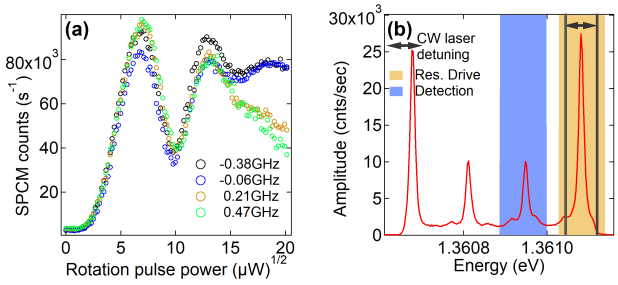


FIG. S9. (a) Rabi Oscillations for different detuning of the CW laser as a function of the pulse power. (b) Quantum dot spectrum showing the frequency scan of the CW laser across the targeted optical transition, with the black vertical lines indicating the detuning range used in the experiment.

to evolve slightly along either an upward or a downward trend (Fig. S9(a)).

This behavior was observed consistently while stepping the CW laser frequency across the transition and repeating the pulsed-control measurements (Fig. S9(b)), suggesting that the nuclear environment is not merely a passive source of quasi-static noise, but is instead influenced by the optical driving conditions. In addition, when the CW laser is set slightly off resonance, while keeping the pulse parameters and detection configuration unchanged, the Ramsey fringe visibility can increase relative to exact resonance (Fig. S10). We attribute the observed dependence on CW-laser detuning to dynamic nuclear polarisation (DNP) induced by resonant optical cycling. Optically driven nuclear-spin polarisation is well established in semiconductor quantum dots and has been demonstrated under resonant excitation in the Voigt geometry, where the hyperfine interaction between the optically driven carrier spin and the nuclear-spin bath generates an effective Overhauser field [6–8]. In particular, resonant nuclear-spin pumping has been observed in singly charged (In,Ga)As/GaAs quantum dots subject to a transverse magnetic field [7, 9]. In this regime, the optically induced nuclear polarisation can modify the effective magnetic field experienced by the confined carrier [9–11], thereby affecting its spin splitting and dynamics. Moreover, DNP has been shown to depend on the optical excitation conditions and to produce detuning-dependent resonance shifts or "dragging" of the optical transition [8]. We therefore interpret the observed changes in the Rabi response and Ramsey coherence with CW detuning as arising, at least in part, from changes in the nuclear polarisation and the corresponding Overhauser field.

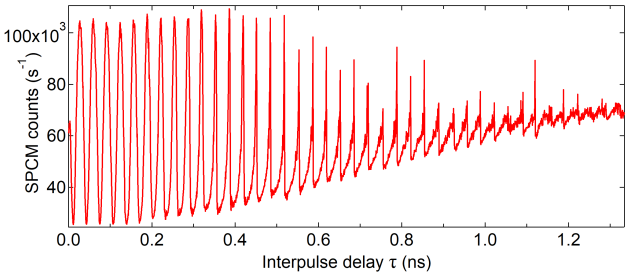


FIG. S10. Ramsey fringes for a slightly modified resonant-laser detuning (~ -0.4 GHz from "resonance"), showing enhanced coherence times. For delays above 500 ps, the fringes acquire the characteristic sawtooth-like form, attributed to DNP effects.

[1] K. Barr, B. Hourahine, C. Schneider, S. Höfling, and K. G. Lagoudakis, Towards spin state tailoring of charged excitons in ingaas quantum dots using oblique magnetic fields, Phys. Rev. B **109**, 075433 (2024).

[2] K. J. Nash, M. S. Skolnick, P. A. Claxton, and J. S. Roberts, Diamagnetism as a probe of exciton localization in quantum wells, Phys. Rev. B **39**, 10943 (1989).

[3] B. Van Hattem, P. Corfdir, P. Brereton, P. Pearce, A. M. Graham, M. J. Stanley, M. Hugues, M. Hopkinson, and R. T. Phillips, From the artificial atom to the kondo-anderson model: Orientation-dependent magnetophotoluminescence of charged excitons in inas quantum dots, Phys. Rev. B **87**, 205308 (2013).

[4] J. van Bree, A. Y. Silov, M. L. van Maasakkers, C. E. Pryor, M. E. Flatté, and P. M. Koenraad, Anisotropy of electron and hole g tensors of quantum dots: An intuitive picture based on spin-correlated orbital currents, Phys. Rev. B **93**, 035311 (2016).

[5] B. Schaefer, E. Collett, R. Smyth, D. Barrett, and B. Fraher, Measuring the Stokes polarization parameters, American Journal of Physics **75**, 163 (2007).

[6] E. A. Chekhovich, M. N. Makhonin, A. I. Tartakovskii, A. Yacoby, H. Bluhm, K. C. Nowack, and L. M. K. Vandersypen, Nuclear spin effects in semiconductor quantum dots, Nature Mater **12**, 494 (2013).

[7] R. V. Cherbunin, K. Flisinski, I. Y. Gerlovin, I. V. Ignatiev, M. S. Kuznetsova, M. Y. Petrov, D. R. Yakovlev, D. Reuter, A. D. Wieck, and M. Bayer, Resonant nuclear spin pumping in (in,ga)as quantum dots, Phys. Rev. B **84**, 041304(R) (2011).

[8] R. Stockill, C. Le Gall, C. Matthiesen, L. Huthmacher, E. Clarke, M. Hugues, and M. Atatüre, Quantum dot spin coherence governed by a strained nuclear environment, Nat Commun **7**, 12745 (2016).

[9] T. D. Ladd, D. Press, K. De Greve, P. L. McMahon, B. Friess, C. Schneider, M. Kamp, S. Höfling, A. Forchel, and Y. Yamamoto, Pulsed nuclear pumping and spin diffusion in a single charged quantum dot, Phys. Rev. Lett. **105**, 107401 (2010).

[10] S. E. Economou and E. Barnes, Theory of dynamic nuclear polarization and feedback in quantum dots, Phys. Rev. B **89**, 165301 (2014).

[11] P. Millington-Hotze, H. E. Dyte, S. Manna, S. F. Covre da Silva, A. Rastelli, and E. A. Chekhovich, Approaching a fully-polarized state of nuclear spins in a solid, Nat Commun **15**, 985 (2024).